Mitofusins *Mfn1* and *Mfn2* Are Required to Preserve Glucose- but Not Incretin-Stimulated β-Cell Connectivity and Insulin Secretion

Eleni Georgiadou,[1] Charanya Muralidharan,[2] Michelle Martinez,[2] Pauline Chabosseau,[1] Elina Akalestou,[1] Alejandra Tomas,[1] Fiona Yong Su Wern,[3] Theodoros Stylianides,[4] Asger Wretlind,[5] Cristina Legido-Quigley,[5,6] Ben Jones,[7] Livia Lopez-Noriega,[1] Yanwen Xu,[8] Guoqiang Gu,[8] Nour Alsabeeh,[9] Céline Cruciani-Guglielmacci,[10] Christophe Magnan,[10] Mark Ibberson,[11] Isabelle Leclerc,[1] Yusuf Ali,[3] Scott A. Soleimanpour,[12,13] Amelia K. Linnemann,[2] Tristan A. Rodriguez,[14] and Guy A. Rutter[1,3,15]

Diabetes 2022;71:1472–1489 | https://doi.org/10.2337/db21-0800

Mitochondrial glucose metabolism is essential for stimulated insulin release from pancreatic β-cells. Whether mitofusin gene expression, and hence, mitochondrial network integrity, is important for glucose or incretin signaling has not previously been explored. Here, we generated mice with β-cell–selective, adult-restricted deletion knock-out (dKO) of the mitofusin genes *Mfn1* and *Mfn2* (β*Mfn1/2* dKO). β*Mfn1/2*-dKO mice displayed elevated fed and fasted glycemia and a more than fivefold decrease in plasma insulin. Mitochondrial length, glucose-induced polarization, ATP synthesis, and cytosolic and mitochondrial Ca^{2+} increases were all reduced in dKO islets. In contrast, oral glucose tolerance was more modestly affected in β*Mfn1/2*-dKO mice, and glucagon-like peptide 1 or glucose-dependent insulinotropic peptide receptor agonists largely corrected defective glucose-stimulated insulin secretion through enhanced EPAC-dependent signaling. Correspondingly, cAMP increases in the cytosol, as measured with an Epac-camps–based sensor, were exaggerated in dKO mice. Mitochondrial fusion and fission cycles are thus essential in the β-cell to maintain normal glucose, but not incretin, sensing. These findings broaden our understanding of the roles of mitofusins in β-cells, the potential contributions of altered mitochondrial dynamics to diabetes development, and the impact of incretins on this process.

Mitochondria are often referred to as the powerhouses or "chief executive organelles" of the cell, using fuels to provide most of the energy required to sustain normal function (1). Mitochondrial oxidative metabolism plays a pivotal role in the response of pancreatic β-cells to stimulation by glucose and other nutrients (2). Thus, as blood

[1]Section of Cell Biology and Functional Genomics, Division of Diabetes, Endocrinology and Metabolism, Department of Medicine, Imperial College London, London, U.K.
[2]Center for Diabetes and Metabolic Diseases, Indiana University School of Medicine, Indianapolis, IN
[3]Lee Kong Chian School of Medicine, Nanyang Technological University, Singapore
[4]Centre of Innovative and Collaborative Construction Engineering, Loughborough University, Leicestershire, U.K.
[5]Systems Medicin, Steno Diabetes Center Copenhagen, Copenhagen, Denmark
[6]Institute of Pharmaceutical Science, Kings College London, London, U.K.
[7]Section of Endocrinology and Investigative Medicine, Imperial College, London, U.K.
[8]Department of Cell and Developmental Biology, Program of Developmental Biology, and Vanderbilt Center for Stem Cell Biology, Vanderbilt University, School of Medicine, Nashville, TN
[9]Department of Physiology, Health Sciences Center, Kuwait University, Kuwait City, Kuwait
[10]Regulation of Glycemia by Central Nervous System, Université de Paris, BFA, UMR 8251, CNRS, Paris, France
[11]Vital-IT Group, SIB Swiss Institute of Bioinformatics, Lausanne, Switzerland
[12]Division of Metabolism, Endocrinology & Diabetes and Department of Internal Medicine, University of Michigan Medical School, Ann Arbor, MI
[13]Veterans Affairs Ann Arbor Healthcare System, Ann Arbor, MI
[14]Imperial Centre for Translational and Experimental Medicine, National Heart and Lung Institute, Imperial College London, London, U.K.
[15]Centre of Research of Centre Hospitalier de l'Université de Montréal (CHUM), University of Montreal, Montreal, Quebec, Canada

Corresponding author: Guy A. Rutter, g.rutter@imperial.ac.uk or guy.rutter@umontreal.ca

Received 3 September 2021 and accepted 4 April 2022

This article contains supplementary material online at https://doi.org/10.2337/figshare.19607232.

glucose increases, enhanced glycolytic flux and oxidative metabolism lead to an increase in ATP synthesis, initiating a cascade of events that involve the closure of K_{ATP} channels (3), plasma membrane depolarization, and the influx of Ca^{2+} via voltage-dependent Ca^{2+} channels (VDCC). The latter, along with other less well-defined "amplifying" signals (4), drive the biphasic release of insulin (2). Gut-derived incretin hormones, including glucagon-like peptide-1 (GLP-1) and glucose-dependent insulinotropic peptide (GIP) (5), further potentiate secretion by binding to class-B G protein-coupled receptors (GPCRs) to generate cAMP and other intracellular signals (5).

Under normal physiological conditions, mitochondria undergo fusion and fission cycles that are essential for quality control and adaptation to energetic demands (6). Thus, highly interconnected mitochondrial networks allow communication and interchange of contents between mitochondrial compartments as well as with other organelles such as the endoplasmic reticulum (ER) (7). These networks exist interchangeably with more fragmented structures, displaying more "classical" mitochondrial morphology (8). Mitochondrial fission is also necessary for "quality control" and the elimination of damaged mitochondria by mitophagy (9).

While the mitofusins MFN1 and MFN2, homologs of the *Drosophila melanogaster* fuzzy onions (*fzo*) and mitofusin (*dmfn*) gene products (10), are guanosine-5'-triphosphatases that mediate fusion of the outer mitochondrial membrane, optic atrophy protein 1 (OPA1) controls that of the inner mitochondrial membrane. Dynamin-related protein 1 (DRP1) is responsible for mitochondrial fission (11). Other regulators include mitochondrial fission 1 protein (FIS1), mitochondrial fission factor (MFF), and MiD49/51 (12).

Earlier studies (13–18) have shown that perturbations in mitochondrial structure in β-cells have marked effects on glucose-stimulated insulin secretion (GSIS). Surprisingly, whether the canonical and evolutionarily conserved machinery involved in mitochondrial fusion (i.e., the mitofusins), control mitochondrial structure in β-cells has not been explored yet. Furthermore, none of the earlier studies have investigated the actions of mitochondrial structure destruction in adult mice. Finally, whether and to what extent they impact secretion stimulated by other agents, including incretins, is less clear. This question is important given that changes in mitochondrial oxidative metabolism (19) and structure contribute to type 2 diabetes (T2D).

Here, we first explored the potential contribution of mitofusins to the effects of diabetic conditions. We next determined whether deletion of *Mfn1* and *Mfn2* in β-cells in adult mice may impact insulin secretion. Lastly, we aimed to determine whether incretins may rescue or bypass any observed perturbations. We show that mitofusin ablation exerts profound effects on insulin release, glucose homeostasis, and Ca^{2+} dynamics. Remarkably, the deficiencies in insulin secretion are largely corrected by incretin hormones. This suggests a possible approach to ameliorating the consequences of mitochondrial fragmentation with these agonists in some forms of diabetes.

RESEARCH DESIGN AND METHODS

Study Approval

C57BL/6J mice were housed in individually ventilated cages in a pathogen-free facility at 22°C with a 10–14-h light-dark cycle and were fed ad libitum with a standard mouse chow diet (Research Diets, New Brunswick, NJ). All in vivo procedures were approved by the U.K. Home Office, according to the Animals (Scientific Procedures) Act 1986 with local ethical committee (Hammersmith Hospital Campus, London, U.K.) approval under personal project license number PA03F7F07 to I.L.

Generation of β-Cell Selective *Mfn1/Mfn2* Knockout, *Clec16a* Null, and Pdx1CreER Mice

C57BL/6J male mice bearing *Mfn1* ($Mfn1^{tm2Dcc}$; JAX stock no. 026401) and *Mfn2* (B6.129(Cg)-$Mfn2^{tm3Dcc}$/J; JAX stock no. 026525; The Jackson Laboratory, Bar Harbor, ME) alleles (20) with *lox*P sites flanking exons 4 and 6 were purchased from The Jackson Laboratory and crossed to C57BL/6J transgenic animals carrying an inducible *Cre* recombinase under *Pdx1* promoter control (Pdx1-Cre^{ERT2}) (21). Mice bearing floxed *Mfn* alleles but lacking *Cre* recombinase were used as littermate controls in this study. Mice were genotyped following protocols described by The Jackson Laboratory for each of these strains (see Supplementary Table 1). Recombination was achieved by daily tamoxifen (10 mg/mouse diluted in corn oil; Sigma-Aldrich, Dorset, U.K.) i.p. injections for 5 days at 7–8 weeks of age in both control and β-cell selective *Mfn1/Mfn2* deletion knockout (dKO) (β*Mfn1/2* dKO) groups.

Animals with floxed *Clec16a* alleles were bred to mice carrying the Pdx1-Cre transgene (*Clec16a*$^{\Delta panc}$), as previously described (22). Pdx1-Cre alone mice were used as littermate controls. Pdx1CreER mice were generated as previously described (21).

RNA Extraction and Quantitative RT-PCR

For measurements of mRNA levels, pancreatic islets from control and β*Mfn1/2*-dKO mice were isolated by collagenase digestion (23). Total RNA from 50 to 100 islets was extracted and underwent quantitative (q)RT-PCR, as previously described (24) (see Supplementary Table 2 for primer details).

Tissue DNA Extraction and Measurement of mtDNA Copy Number

Total islet DNA was isolated using Puregene Cell and Tissue Kit (Qiagen, Manchester, U.K.) and was amplified (100 ng) using NADH dehydrogenase I primers (25), also

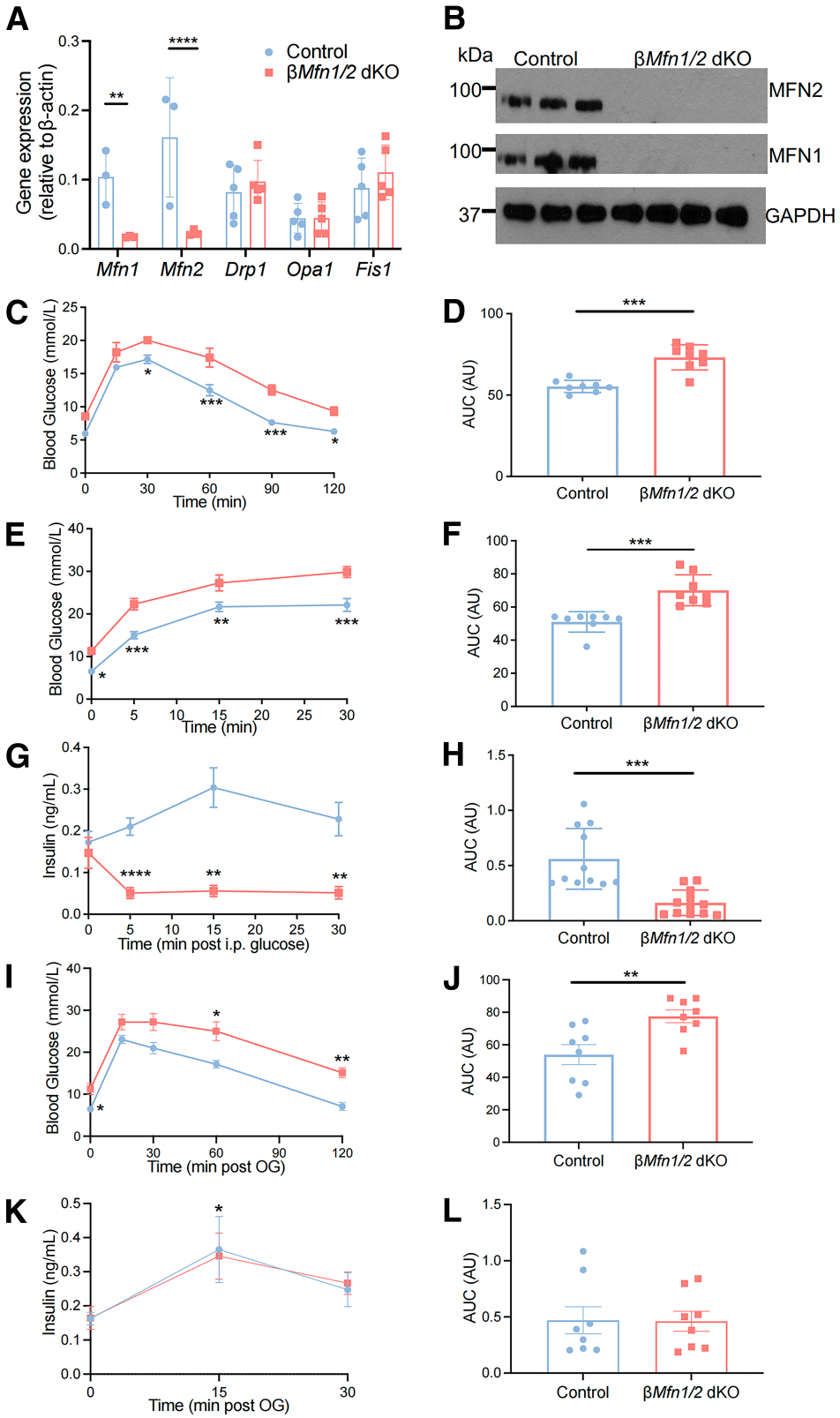

Figure 1—Generation of a conditional β*Mfn1/2*-dKO mouse line, which displays a highly impaired glucose tolerance in vivo. *A*: qRT-PCR quantification of *Mfn1, Mfn2, Drp1, Opa1*, and *Fis1* expression in control and dKO islets relative to *β-actin* (n = 3–5 mice per genotype in two independent experiments). *B*: Western blot analysis demonstrating efficient MFN1 (84 kDa) and MFN2 (86 kDa) deletion relative to GAPDH (36 kDa) in isolated islets (n = 3–4 mice per genotype in three independent experiments). *C*: Glucose tolerance was measured in dKO mice and littermate controls by IPGTT (1 g/kg body wt). *D*: Corresponding area under the curve (AUC; AU, arbitrary units) from (*C*) (n = 8 mice per genotype, in two independent experiments). Glucose tolerance measured by IPGTT (using 3 g/kg body wt) (*E*), and the corresponding AUC (*F*) were assessed in β*Mfn1/2*-dKO and control mice (n = 8 mice per genotype in two independent experiments). Plasma

known as complex I (*mt9/mt11)* for mtDNA and *Ndufv1* for nuclear DNA.

SDS-PAGE and Western Blotting

Islets were collected and lysed (20 μg), as previously described (24). The antibodies used are summarized in Supplementary Table 3.

Intraperitoneal or Oral Gavage of Glucose, Followed by Insulin, Proinsulin, or Ketone Levels Measurement and Insulin Tolerance Test In Vivo

Intraperitonal glucose tolerance tests (IPGTTs), intraperitoneal insulin tolerance tests (IPIITTs), oral glucose tolerance tests (OGTTs), and plasma insulin measurements were performed as previously described (24). Plasma proinsulin levels were measured in fasted (16 h) animals using a rat/mouse proinsulin ELISA kit (Mercodia). Plasma β-ketones were measured from fed or fasted (16 h) mice using an Areo 2K device (GlucoMen, Berkshire, U.K.).

In Vitro Insulin Secretion

Islets were isolated from mice and incubated for 1 h in Krebs-Ringer bicarbonate buffer containing 3 mmol/L glucose, as previously described (24).

Single-Cell Fluorescence Imaging

Dissociated islets were incubated with 100 nmol/L MitoTracker Green (Thermo Fisher Scientific) in Krebs-Ringer bicarbonate buffer containing 11 mmol/L glucose for 30 min. MitoTracker Green was then washed with Krebs buffer with 11 mmol/L glucose before fluorescence imaging. Experiments with tetramethylrhodamine ethyl ester (TMRE) were performed as previously described (24). Clusters of dissociated islets were transduced for 48 h with an adenovirus encoding the low-Ca^{2+}-affinity sensor D4 addressed to the ER, Ad-RIP-D4ER (multiplicity of infection: 100), as previously described (26). Bleaching was corrected as previously described (27). Clusters of dissociated islets were transduced for 24 h with an adenovirus encoding Epac1-camps, as previously described (28).

Mitochondrial Shape Analysis

For each stack, one image at the top, middle, and bottom of the islet was analyzed. After background subtraction, the following parameters were measured for each cell: number of particles, perimeter, circularity, elongation (1/circularity), density, and surface area of each particle (29).

Whole-Islet Fluorescence Imaging

Cytosolic and mitochondrial Ca^{2+} imaging as well as ATP-to-ADP changes in whole islets were performed as previously described (24).

TIRF Fluorescence Imaging

Experiments using the membrane-located zinc sensor ZIMIR (50 μmol/L) (30) or the fluorescent genetically encoded and vesicle-located green marker neuropeptide Y (NPY)-Venus were performed as previously described (31).

Pancreas Immunohistochemistry

Isolated pancreata were fixed and imaged as previously described (24). The antibodies used are summarized in Supplementary Table 3. For examination of apoptosis, TUNEL assay was performed using a DeadEnd Fluorometric TUNEL system kit and DNase I treatment (Promega, Madison, WI), according to the manufacturer's instructions.

Metabolomics/Lipidomics

Metabolites were quantified using targeted ultrahigh-performance liquid chromatography coupled with triple quadrupole mass spectrometry, as described earlier (32). Lipidomic sample preparation followed the Folch procedure with minor adjustments. Significance was tested by the Student two-tailed *t* test using GraphPad Prism 8 software.

Measurement of Oxygen Consumption Rate

The oxygen consumption rate (OCR) was measured with XF96 assays (Seahorse Bioscience, Agilent, Santa Clara, CA) using mouse islets (~10 per well), as previously described (33). Parameters were analyzed as previously described (34).

Electron Microscopy

For conventional electron microscopy, islets were fixed and imaged as previously described (35).

Connectivity Analysis

Pearson (r)-Based Connectivity and Correlation Analyses

Correlation analyses in an imaged islet were performed as previously described (36).

insulin levels during IPGTT in dKO and control mice (n = 11–12 mice per genotype in three independent experiments) (*G*), and the corresponding AUC (*H*). *I*: Glucose tolerance after oral gavage (3 g/kg body wt) was measured in eight animals per genotype in two independent experiments. Glucose baseline values between control and dKO mice were significantly different (*$P < 0.05$). Increases in glucose from baseline in control animals were ****$P < 0.0001$, ***$P < 0.001$, and **$P < 0.01$ and were ****$P < 0.0001$ in dKO animals from 15 to 60 min accordingly. *J*: The corresponding AUC. Plasma insulin levels during OGTT in dKO and control mice (n = 8 mice per genotype in two independent experiments) (*K*) and the corresponding AUC (*L*). All experiments were performed in 14-week-old male mice. Data are presented as mean ± SD in *A* and as mean ± SEM in *B–L*. *$P < 0.05$; **$P < 0.01$; ***$P < 0.001$; ****$P < 0.0001$, as indicated, or control vs. dKO mice at the time points as indicated in *K*, analyzed by unpaired two-tailed Student *t* test and Mann-Whitney correction or two-way ANOVA test and the Šidák multiple comparisons test.

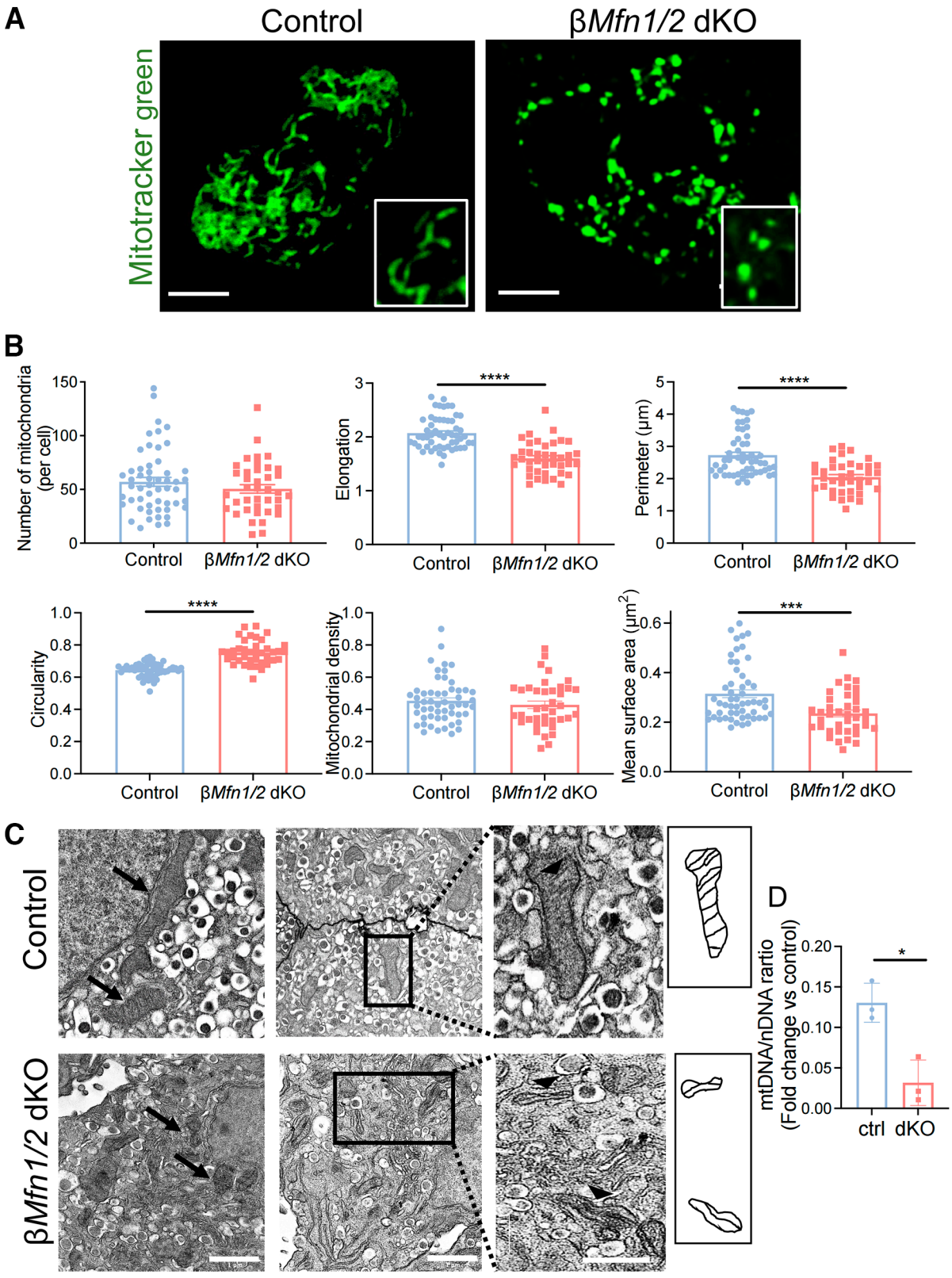

Figure 2—Mitochondrial ultrastructure is altered following *Mfn1/2* deletion. *A*: Confocal images of the mitochondrial network of dissociated β-cells stained with MitoTracker Green; scale bar: 5 μm. Lower right panels: magnification of selected areas. *B*: Mitochondrial morphology analysis on deconvolved confocal images of dissociated β-cells. A macro was developed to quantify the number of mitochondria per cell and measure the elongation, perimeter, circularity (0: elongated; 1: circular mitochondria), density, and surface area of the organelles in control and dKO animals (n = 40–54 cells; n = 3 mice per genotype). *C*: Electron micrographs of mitochondria indicated with black arrows in islets isolated from control and dKO mice; scale bars: 1 μm. Right panel: magnification of selected areas showing the cristae structure (black arrow heads); scale

RNA Sequencing Data Analysis

Processing and differential expression analysis of RNA sequencing data from islets isolated from mice fed a high-fat high-sugar diet (HFHS; D12331, Research Diets) or regular chow (RC) diet (C57Bl/6J, DBA/2J, BALB/cJ, A/J, AKR/J, 129S2/SvPas) was performed as previously described (37) using the *Limma* package in R. *P* values were adjusted for multiple comparisons using the Benjamini-Hochberg procedure (38).

Statistics

Data are expressed as mean ± SD, unless otherwise stated. Significance was tested by the Student two-tailed *t* test and Mann-Whitney correction or two-way ANOVA with the Šidák multiple comparison test for comparison of more than two groups, using GraphPad Prism 9 software (GraphPad Software, San Diego, CA). $P < 0.05$ was considered significant. Experiments were not randomized or blinded.

Data and Resource Availability

The data sets generated and/or analyzed during the current study are available from the corresponding author upon reasonable request. No applicable resources were generated or analyzed during the current study.

RESULTS

Changes in *Mfn1* and *Mfn2* Expression in Mouse Strains Maintained on RC or HFHS Diet

To determine whether the expression of *Mfn1* or *Mfn2* might be affected under conditions of hyperglycemia mimicking T2D in humans, we interrogated data from a previous report (37) in which RNA sequencing was performed on six mouse strains. BALB/cJ mice showed "antiparallel" changes in *Mfn1* and *Mfn2* expression in response to maintenance on an HFHS diet for 10 days, and similar changes were obtained in DBA/2J mice at 30 and 90 days (Supplementary Fig. 1*A* and *B*).

Generation of a Conditional β*Mfn1/2*-dKO Mouse Line

Efficient deletion of *Mfn1* and *Mfn2* in the β-cell was achieved in adult mice using the Pdx1-Cre^{ERT2} transgene and tamoxifen injection at 7–8 weeks. Possession of this transgene, which does not contain the human growth hormone (hGH) cDNA (21), alone had no effect on glycemic phenotype or cellular composition of pancreatic islets (Supplementary Fig. 2*A*–*C*). Deletion of mitofusin genes was confirmed by qRT-PCR (Fig. 1*A*) and Western (immuno-) blotting (Fig. 1*B*) analysis, ∼7 weeks posttamoxifen injection. Relative to *β-actin*, expression of the *Mfn1* and *Mfn2* transcripts in isolated islets from dKO mice decreased by ∼ 83 and 86% accordingly versus control islets (Fig. 1*A*), consistent with selective deletion in the β-cell compartment (39). No differences were detected in the expression of other mitochondrial fission and fusion mediator genes such as *Opa1*, *Drp1*, and *Fis1* in islets (Fig. 1*A*) or in *Mfn1* and *Mfn2* in other relevant tissues (Supplementary Fig. 3*A*). dKO mice were significantly lighter than control animals after 20–21 weeks (Supplementary Fig. 3*B*).

β*Mfn1/2*-dKO Mice Are Glucose Intolerant With Impaired GSIS In Vivo

Glucose tolerance was impaired in dKO mice compared with control littermates at 14 weeks (Fig. 1*C* and *D*), and this difference was further exaggerated at 20 weeks (Supplementary Fig. 3 and Fig. 3*C*). At 14 weeks, β*Mfn1/2*-dKO mice (with a 27 mmol/L glycemia at 15 min) (Fig. 1*E* and *F*) showed a dramatically lower insulin excursion upon glucose challenge versus control animals (Fig 1*G* and *H*). Following an oral gavage, glucose tolerance was more modestly affected in dKO mice (Fig. 1*I* and *J*), while plasma insulin levels in these animals (with a glycemia of 27 mmol/L at 15 min) were indistinguishable from control animals (0 vs. 15 min in dKO) (Fig. 1*K* and *L*). Insulin tolerance was unaltered in β*Mfn1/2*-dKO versus control mice (Supplementary Fig. 3*D*), while proinsulin conversion was impaired (Supplementary Fig. 3*E* and *F*). dKO mice displayed significantly elevated plasma glucose (Supplementary Fig. 3*G*) under both fed and fasted conditions, and β-ketones (ketone bodies) were also elevated in fasted versus control animals (Supplementary Fig. 3*H*), whereas plasma insulin levels were lower (Supplementary Fig. 3*I*). Apparent insulin secretion was also impaired after i.p. injection, with a lower glucose in 14- and 20-week-old dKO versus control mice (Supplementary Fig. 4*A*–*D*). In contrast, plasma insulin levels were not statistically different between control and dKO animals following an OGTT at either age (Supplementary Fig. 4*E*–*H*), although a trend toward lower insulin excursion was evident in dKO mice.

Deletion of *Mfn1/2* Alters Mitochondrial Morphology in β-Cells

While the mitochondrial network was highly fragmented in dKO cells (Fig. 2*A* and inset), the number of mitochondria per cell or density was not altered (Fig. 2*B*). Mitochondrial elongation, perimeter, and surface area were also significantly decreased in β*Mfn1/2*-dKO cells, while circularity was increased (Fig. 2*B*). Transmission electron microscopy confirmed these changes (Fig. 2*C*). Cristae structure and organization were also altered in β*Mfn1/2*-dKO cells, with a single crista often running the length of

bar: 0.5 μm. Schematic representation of enlarged mitochondria. *D*: The relative mitochondrial DNA copy number was measured by determining the ratio of the mtDNA-encoded gene *mt-Nd1* to the nuclear gene *Ndufv1* ($n = 3$ mice per genotype). Experiments were performed in 14-week-old male mice. Data are presented as mean ± SEM in *A*–*C* and as mean ± SD in *D*. *$P < 0.05$, ***$P < 0.001$, ****$P < 0.0001$ as indicated, analyzed by unpaired two-tailed Student *t* test and Mann-Whitney correction.

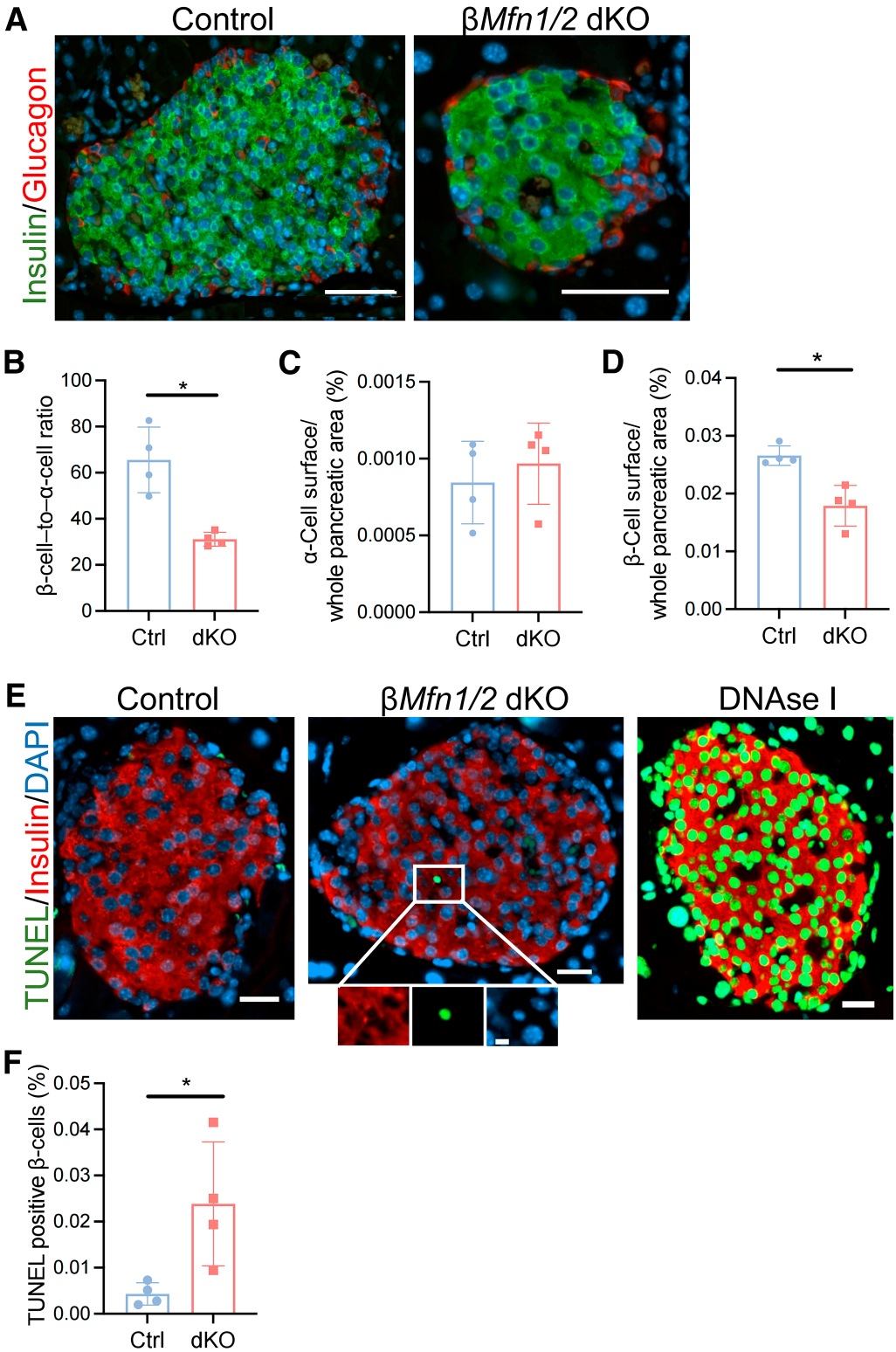

Figure 3—Absence of *Mfn1/2* in β-cells leads to decreased β-cell mass and increased β-cell apoptosis. *A*: Representative pancreatic sections immunostained with glucagon (red) and insulin (green); scale bars: 50 μm. The β-cell and α-cell surface (*B*) measured within the whole pancreatic area in control and dKO mice were determined (*C*), as well as the β-cell–to–α-cell ratio in *D* (n = 79–86 islets, four mice per genotype; experiment performed in triplicate). *E*: Representative confocal images of islets with TUNEL-positive (green) apoptotic β-cells (region of interest) and insulin (red). Magnification of selected area displaying each fluorescent channel; scale bar: 5 μm. DNase I-treated sections were used as a positive control in the TUNEL assay. Scale bars: 20 μm. *F*: Quantification of the percentage of islets containing TUNEL-positive cells (n = 114–133 islets, four mice per genotype; experiment performed in triplicate). Experiments were performed in 14-week-old male mice. Data are presented as mean ± SD. *$P < 0.05$, assessed by unpaired two-tailed Student t test and Mann-Whitney correction.

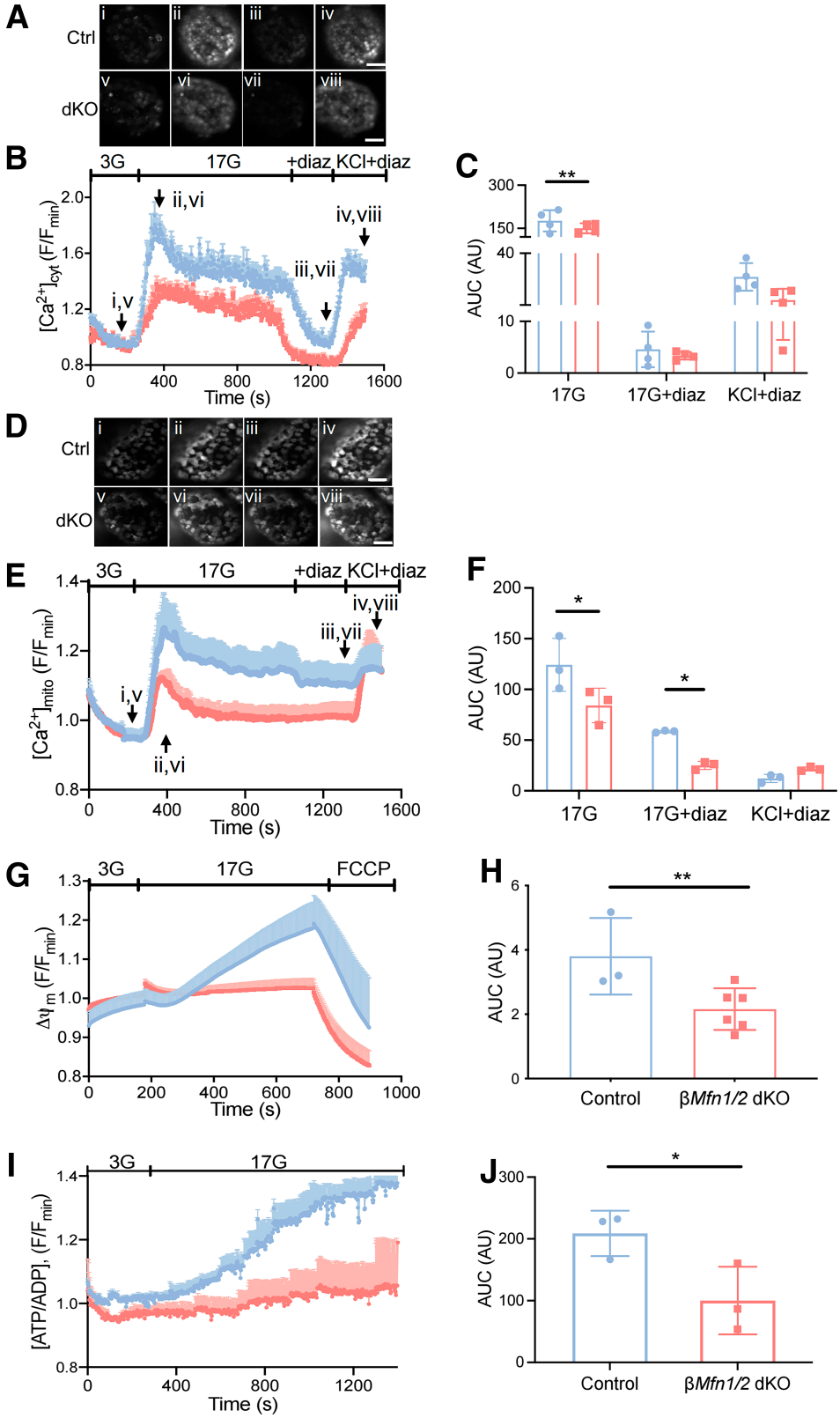

Figure 4—*Mfn1/2* deletion from pancreatic β-cells impairs cytosolic and mitochondrial Ca^{2+} uptake and changes mitochondrial potential and ATP synthesis in vitro. *A*: Each snapshot of isolated control (i–iv) and dKO-derived (v–viii) islets was taken during the time points indicated by the respective arrows in *B*. Scale bar: 50 μm. See also Supplementary Video 1. *B*: $[Ca^{2+}]_{cyt}$ traces in response to 3 mmol/L glucose (3G), 17 mmol/L glucose (17G), with or without 100 μmol/L diazoxide (diaz), or 20 mmol/L KCl with diaz were assessed following Cal-520 uptake in whole islets. Traces represent mean normalized fluorescence intensity over time (F/F_{min}). *C*: The corresponding area under the curve (AUC) is also presented (AU, arbitrary units) (*n* = 17–26 islets, four mice per genotype); 17G AUC was measured between

a mitochondrial section. Finally, dKO islets displayed an ∼5% reduction in mtDNA (Fig. 2*D*).

Mitofusin Deletion Leads to Modest Changes in β-Cell Mass

Pancreatic β-cell mass decreased by 33%, whereas α-cell mass was not affected in dKO mice (Fig. 3*A–C*). The β-cell–to–α-cell ratio was decreased by 53% (Fig. 3*D*), in line with an increase in TUNEL-positive β-cells in dKO versus control animals (Fig. 3*E* and *F*).

Mitochondrial Fragmentation, β-Cell Mass Deterioration, and Hyperglycemia Emerge in dKO Mice 2 Weeks After Tamoxifen Administration

We next sought to exclude the possibility that mitochondrial fragmentation may simply be the consequence of the observed hyperglycemia. Two distinct groups of organelles (both elongated and circular) were apparent in β*Mfn1/2*-dKO cells (Supplementary Fig. 5*A* and *B*) 2 weeks after tamoxifen treatment. Neither fed nor fasted glycemia or plasma insulin levels following glucose challenge were different between groups (Supplementary Fig. 5*C–E*). A trend toward lower β-cell mass and mtDNA was detected in dKO animals (Supplementary Fig. 5*F–I*).

β-Cell Identity Is Modestly Altered in β*Mfn1/2*-dKO Islets

While *Ins2*, *Ucn3*, and *Glut2* (*Slc2a2*) were significantly downregulated, *Trpm5* was upregulated in dKO islets (Supplementary Fig. 6). No changes in α- or β-cell disallowed genes (40) were detected. In contrast, genes involved in mitochondrial function, such as *Smdt1* and *Vdac3*, were upregulated in dKO β-cells (Supplementary Fig. 6). Lastly, genes involved in ER stress and mito/autophagy were also affected, with *Chop (Ddit3)* and *p62* being upregulated and *Lc3* and *Cathepsin L* downregulated.

Mitofusins Are Essential to Maintain Normal Glucose-Stimulated Ca^{2+} Dynamics, Mitochondrial Membrane Potential, and ATP Levels

Increased cytosolic Ca^{2+} is a key trigger of insulin exocytosis in response to high glucose (2). dKO mouse islets exhibited a significantly smaller glucose-induced $[Ca^{2+}]_{cyt}$ rise versus control islets (Fig. 4*A–C*). When the K_{ATP} channel opener diazoxide and a depolarizing K^+ concentration were then deployed together to bypass the regulation of these channels by glucose, cytosolic Ca^{2+} increases were not significantly impaired in dKO compared with control animals (Fig. 4*B* and *C*). A substantial reduction in mitochondrial free Ca^{2+} concentration ($[Ca^{2+}]_{mito}$) in response to 17 mmol/L glucose (24) was also observed in dKO islets (Fig. 4*D–F*). Of note, subsequent hyperpolarization of the plasma membrane with diazoxide caused the expected lowering of mitochondrial $[Ca^{2+}]_{mito}$ in control islets, reflecting the decrease in $[Ca^{2+}]_{cyt}$ (Fig. 4*E* and *F*), but was almost without effect on dKO islets.

Glucose-induced increases in $\Delta\psi_m$ were also sharply reduced in dKO versus control mouse islets (Fig. 4*G* and *H*). Addition of 2-[2-[4-(trifluoromethoxy)phenyl]hydrazinylidene]-propanedinitrile (FCCP) resulted in a similar collapse in apparent $\Delta\psi_m$ in islets from both genotypes (Fig. 4*G*). Cytosolic Ca^{2+} oscillations and synchronous $\Delta\psi_m$ depolarization were also largely abolished in response to glucose in dKO cells when measured by intravital imaging in vivo (41). Finally, to assess whether deletion of *Mfn1* and *Mfn2* may impact glucose-induced increases in mitochondrial ATP synthesis, we performed real-time fluorescence imaging using Perceval (Fig. 4*I* and *J*). While control islets responded with a time-dependent rise in the ATP-to-ADP ratio in response to a step increase in glucose from 3 mmol/L to 17 mmol/L, β*Mfn1/2*-dKO β-cells failed to mount any response (Fig. 4*J*).

β-Cell–β-Cell Connectivity Is Impaired by *Mfn1/2* Ablation

Intercellular connectivity is required in the islet for a full insulin secretory response to glucose (42). To assess this, individual Ca^{2+} traces recorded from Cal-520–loaded β-cells in mouse islets (Fig. 4*A* and *B*) were subjected to correlation (Pearson *r*) analysis to map cell-to-cell connectivity (Supplementary Fig. 7*A*). Following perfusion at 17 mmol/L glucose, β*Mfn1/2*-dKO β-cells tended to display an inferior, although not significantly different, coordinated activity than control cells, as assessed by counting the number of coordinated cell pairs (0.94 vs. 0.90 for control

245 s and 1,045 s, 17G+diaz AUC was measured between 1,200 s and 1,320 s, and KCl+diaz AUC was measured between 1,424 s and 1,500 s. For each genotype, different baselines (ctrl diaz/KCl: 0.95, dKO diaz/KCl: 0.8) were taken into consideration to measure AUCs. *D*: Each snapshot of isolated control (i–iv) and dKO-derived (v–viii) islets was taken during the time points indicated by the respective arrows in *E*. Scale bar: 50 μm. See also Supplementary Video 2. *E*: $[Ca^{2+}]_{mito}$ changes in response to 17G, with or without diaz, and 20 mmol/L KCl were assessed in islets following R-GECO infection. Traces represent mean normalized fluorescence intensity over time (F/F_{min}), where F_{min} is the mean fluorescence recorded during imaging under 3G. *F*: The corresponding AUC is also shown (n = 20–23 islets, three mice per genotype); 17G AUC was measured between 270 s and 1,100 s, 17G+diaz AUC was measured between 1,101 s and 1,365 s, and KCl AUC was measured between 1,366 s and 1,500 s. *G*: Dissociated β-cells were loaded with TMRE to measure changes in $\Delta\psi_m$ and perifused with 3G, 17G, or FCCP, as indicated. Traces represent normalized fluorescence intensity over time (F/Fmin). *H*: AUC was measured between 700 s and 730 s (under 17G exposure) from the data shown in *G* (n = 146–254 cells, three to six mice per genotype). *I*: Changes in the cytoplasmic ATP-to-ADP ratio in response to 17G was examined in whole islets using the ATP sensor Perceval. *J*: AUC values corresponding to *I* were measured between 418 s and 1,400 s (under 17G exposure) (data points from n = 22–23 islets, three to six mice per genotype). Experiments were performed in 14-week-old male mice. Data are presented as mean ± SD. $^*P < 0.05$, $^{**}P < 0.01$, assessed by unpaired two-tailed Student *t* test and Mann-Whitney correction or two-way ANOVA test and the Šidák multiple comparisons test.

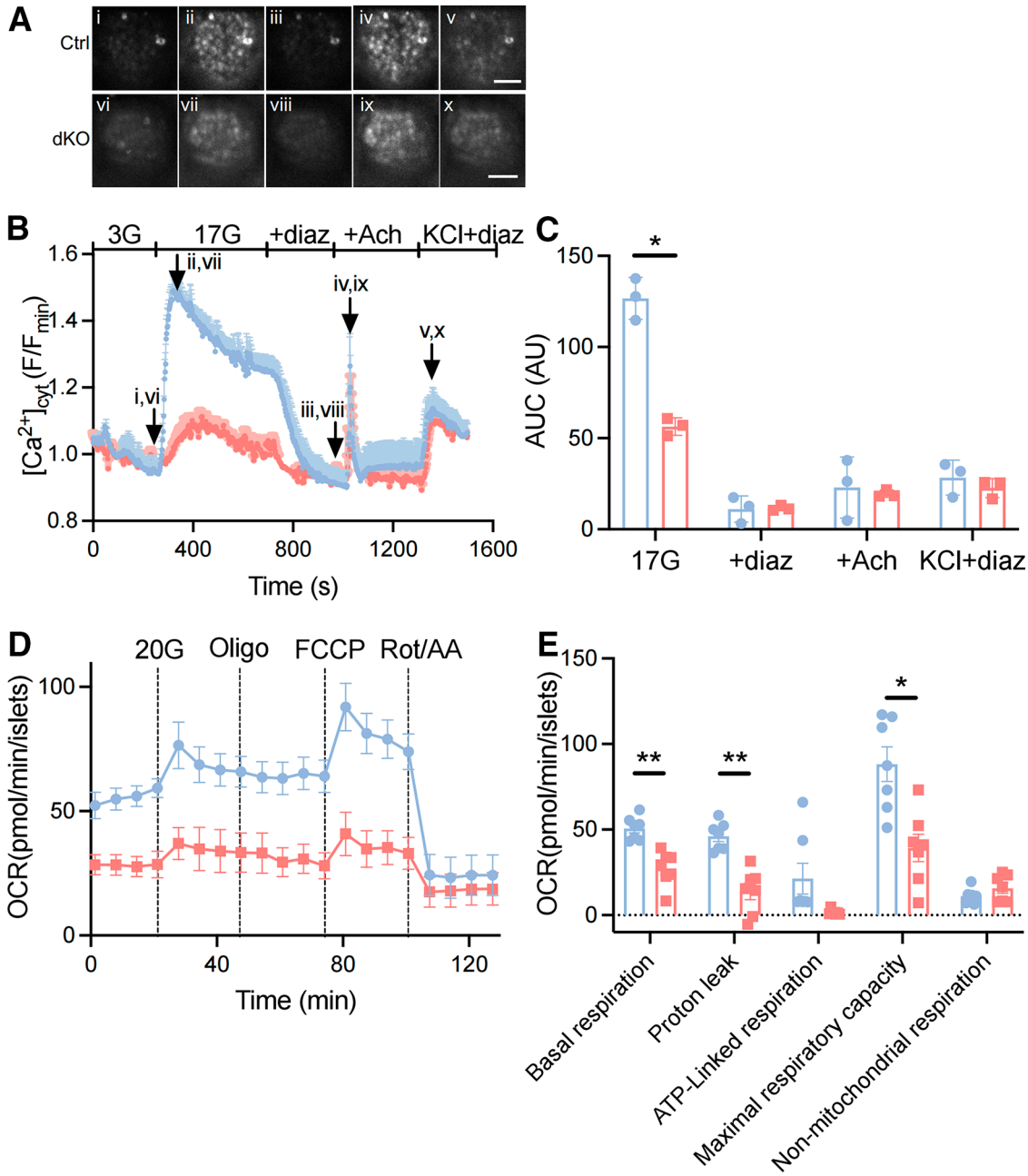

Figure 5—VO_2 and mtDNA are deleteriously affected when *Mfn1/2* are abolished in β-cells, while $[Ca^{2+}]_{ER}$ mobilization remains unchanged. *A*: Each snapshot of isolated control (i–v) and dKO-derived (vi–x) islets was taken during the time points indicated by the respective arrows in *B*. Scale bar: 50 μm. See also Supplementary Video 3. *B*: Changes in $[Ca^{2+}]_{ER}$ were measured in whole islets incubated with Cal-520 and perifused with 17 mmol/L glucose (17G), with or without diazoxide (diaz), 17G with 100 μmol/L acetylcholine (Ach) and diaz, or 20 mmol/L KCl with diaz. *C*: Area under the curve (AUC) values (AU, arbitrary units) corresponding to *B* were measured: 17G AUC was measured between 260 s and 740 s, 17G+diaz AUC was measured between 846 s and 1,020 s, 17G+diaz+Ach AUC was measured between 1,021 s and 1,300 s, and KCl AUC was measured between 1,301 s and 1,500 s (n = 29–31 islets, three mice per genotype). *D*: Representative OCR traces of islets (~10 per well) were acutely exposed to 20 mmol/L glucose (final concentration), 5 μmol/L oligomycin A (Oligo), 1 μmol/L FCCP, and 5 μmol/L rotenone (Rot) with antimycin A (AA) (performed in n = 7 mice, in two independent experiments). *E*: Mitochondrial metabolic parameters were extracted from the OCR traces shown in *D*. Experiments were performed in 14-week-old male mice. Data are presented as mean ± SD in *A–C* and as mean ± SEM in *D* and *E*. *$P < 0.05$,**$P < 0.01$, assessed by the unpaired two-tailed Student *t* test and Mann-Whitney correction or two-way ANOVA test and the Šidák multiple comparisons test.

vs. dKO, respectively) (Supplementary Fig. 7*C*). By contrast, β-cells displayed highly coordinated Ca^{2+} responses upon addition of 20 mmol/L KCl in dKO islets. Similarly, analysis of correlation strength in the same islets revealed significant differences in response to 17 mmol/L glucose between genotypes. In fact, dKO islets had weaker mean

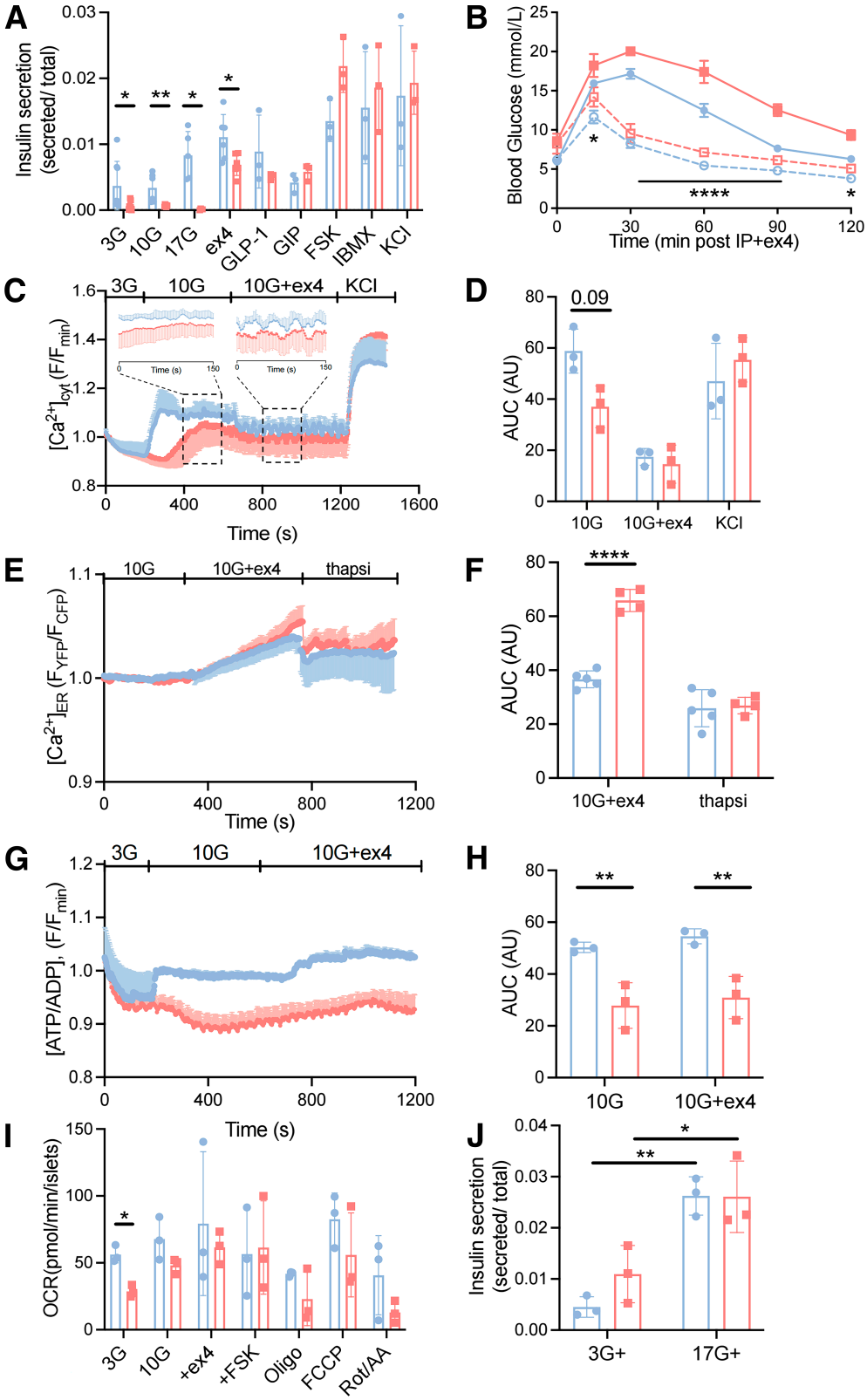

Figure 6— Impaired insulin secretion can be rescued by GLP-1R agonists in vitro by increasing cytosolic Ca^{2+} oscillation frequency. *A*: Insulin secretion measured during serial incubations in batches in 3 mmol/L glucose (3G), 10 mmol/L glucose (10G), 17 mmol/L glucose (17G), 10G supplemented with 100 nmol/L exendin-4 (ex4), GLP-1, GIP, 10 μmol/L FSK, 100 μmol/L IBMX, or 3G with 20 mmol/L KCl (n = 3–7 mice per genotype in two independent experiments; control: 3G vs. ex4, $P < 0.05$; and dKO: 3G vs. ex4, $P < 0.0001$; or 3G vs. GLP-1, $P < 0.001$; or 3G vs. GIP, $P < 0.001$). *B*: Glucose tolerance measured by i.p. coinjection of 1 g/kg glucose and 3 nmol/kg ex4 were assessed in β*Mfn1/2*-dKO and control mice (n = 4–5 mice per genotype, dotted lines). *C*: $[Ca^{2+}]_{cyt}$ changes in response to 3G, 10G, with or without exendin-4 (ex4), or 20 mmol/L KCl were assessed following Cal-520 uptake in whole islets. Traces represent mean normalized

β-cell–to–β-cell coordinated activity (0.88 vs. 0.77 for control vs. dKO, respectively; $P < 0.05$) (Supplementary Fig. 7*B* and *D*), indicating that mitofusins affect the strength of connection rather than the number of coordinated β-cell pairs. A tendency toward lower expression of the gap junction gene *Cx36/Gjd2* was observed in dKO islets (Supplementary Fig. 7*E*). β-Cell "hub" and "leader" distributions (43) were also impaired in the dKO group (data not shown; see [41]).

Unaltered ER Ca^{2+} Mobilization but Decreased Mitochondrial VO_2 and mtDNA Depletion in β*Mfn1/2*-dKO Islets

No differences in cytosolic Ca^{2+} responses between genotypes were observed after agonism at the Gq-coupled metabotropic acetylcholine (Ach) receptor (44,45) (Fig. 5*A–C*). In contrast, measurements of VO_2 revealed that basal, proton leak, and maximal respiratory capacities were significantly impaired in dKO islets (Fig. 5*D* and *E*).

Impaired GSIS In Vitro and β-Cell Connectivity Can Be Rescued by Incretins in β*Mfn1/2*-dKO Mouse Islets

While GSIS was markedly impaired in dKO islets (Fig. 6*A* and Supplementary Table 4), incretins (GLP-1 or GIP), or the GLP1R agonist exendin-4, at a submaximal concentration of 10 mmol/L glucose, led to a significant potentiation in GSIS in both groups. Consequently, insulin secretion in response to 10 mmol/L glucose was no longer different between control and β*Mfn1/2*-dKO islets after incretin addition (Fig. 6*A* and *B*). Moreover, under these conditions, forced increases in intracellular cAMP imposed by the addition of forskolin (FSK) or 3-isobutyl-1-methylxanthine (IBMX), which activate adenylate cyclase (AC) and inhibit phosphodiesterase, respectively, eliminated differences in GSIS between the genotypes (Fig. 6*B*). No differences in insulin secretion were observed between control and dKO islets after depolarization with KCl.

We next explored whether the incretin-mediated improvements in insulin secretion in response to incretins were the result of altered $[Ca^{2+}]_{cyt}$ dynamics. Islets from isolated dKO mice displayed a delayed increase in $[Ca^{2+}]_{cyt}$ in response to 10 mmol/L glucose compared with control islets (Fig. 6*C* and *D*). Addition of exendin-4 led to the emergence of oscillatory activity in both groups, and under these conditions, differences between genotypes, as seen in Fig. 4*B*, were no longer evident (Fig. 6*C*). Measured at 10 mmol/L glucose, control and dKO islets displayed increases in ER Ca^{2+} in response to exendin-4 (Fig. 6*E* and *F*), while the response was exaggerated in the latter group. Neither group displayed significant changes in the ATP-to-ADP ratio in response to exendin-4 (Fig. 6*G* and *H*). Analysis of the OCR revealed no significant differences between genotypes at 10 mmol/L glucose in the presence or absence of exendin-4 or FSK (Fig. 6*I*).

Moreover, mitofusin deletion may lead to a partial activation of "amplification" pathways of GSIS (46) at 3 mmol/L glucose since insulin secretion was enhanced in dKO islets after depolarization of the plasma membrane with KCl in the presence of diazoxide (Fig. 6*J*). Conversely, no differences between islet genotypes were observed at 17 mmol/L glucose (Fig. 6*J*).

While glucose-induced β-cell–β-cell connectivity, as assessed by monitoring Ca^{2+} dynamics (Fig. 6*C*), was markedly impaired in dKO islets (Fig. 7*A* and Supplementary Fig 7), these differences were largely abolished in the presence of exendin-4 (Fig. 8*B–D*).

Insulin Secretion Is Rescued by Incretins Through an EPAC-Dependent Activation

To explore the actions of mitochondrial disruption on incretin signaling, we next used a pharmacological approach. GSIS was more strongly enhanced in dKO versus control islets by IBMX, FSK, or the protein kinase A (PKA) inhibitor H89 alone (Fig. 8*A* and Supplementary Table 4). Selective activation of EPAC also tended to lead to a larger increase in insulin secretion in dKO than in control islets, and this difference became significant when PKA was inhibited with H89 (Fig. 8*B*).

Glucose-dependent increases in cytosolic cAMP, assessed using the Epac-camps sensor, were also markedly amplified in dKO versus control cells (Fig. 8*C* and *D*). This difference persisted in the presence of IBMX and FSK, added separately or alone (Fig. 8*C* and *E*). No changes in

fluorescence intensity over time (F/F_{min}). See also Supplementary Video 4. Dashed regions of interest represent fluorescent segments of extended time scales. Both control and dKO traces reveal faster oscillatory frequencies in response to exendin-4. *D*: The corresponding area under the curve (AUC) is also presented (AU, arbitrary units) (n = 19–20 islets, three mice per genotype). The 10G AUC was measured between 200 s and 660 s, 10G+ex4 AUC was measured between 800 s and 950 s, and KCl AUC was measured between 1,200 s and 1,500 s (AUC 10G: control vs. dKO, $P = 0.09$; AUC control: 10G vs. ex4, $P < 0.05$; AUC dKO: 10G vs. ex4, $P < 0.001$; ex4 vs. KCl, $P < 0.05$). *E*: Dissociated β-cells were transfected with D4ER to measure changes in $[Ca^{2+}]_{ER}$, and perifused with 10G, 10G+ex4, or thapsigargin (10G+thapsi), as indicated. Traces represent corrected ratio values postlinear fitting over time. *F*: AUC was measured between 350 s and 900 s (under 10G+ex4) and between 900 s and 1,300 s (10G+thapsi) from the data shown in *E* (n = 44–46 cells, four to five mice per genotype). G: Changes in cytoplasmic ATP-to-ADP ratio in response to 10G or 10G with 100 nmol/L ex4 was examined in whole islets. *H*: AUC values corresponding to *G* were measured between 185 s and 720 s (under 10G exposure) or between 721 s and 1,200 s (under 10G with ex4) (data points from n = 3 mice per genotype). *I*: Average OCR values of islets (~10 per well) that were exposed to 3G or 10G (final concentration), 10G supplemented with ex4, FSK, oligomycin A (Oligo), FCCP, and rotenone (Rot) with antimycin A (AA) (n = 3 mice per genotype; experiment performed in duplicate). *J*: Insulin secretion measured during serial incubations in batches in 3G or 17G supplemented with 100 μmol/L diazoxide and 30 mmol/L KCl, (n = 3 mice per genotype in two independent experiments). Experiments were performed in 14-week-old male mice. Data are presented as mean ± SD. *$P < 0.05$, **$P < 0.01$, ****$P < 0.0001$, assessed by two-way ANOVA test and the Šidák multiple comparisons test.

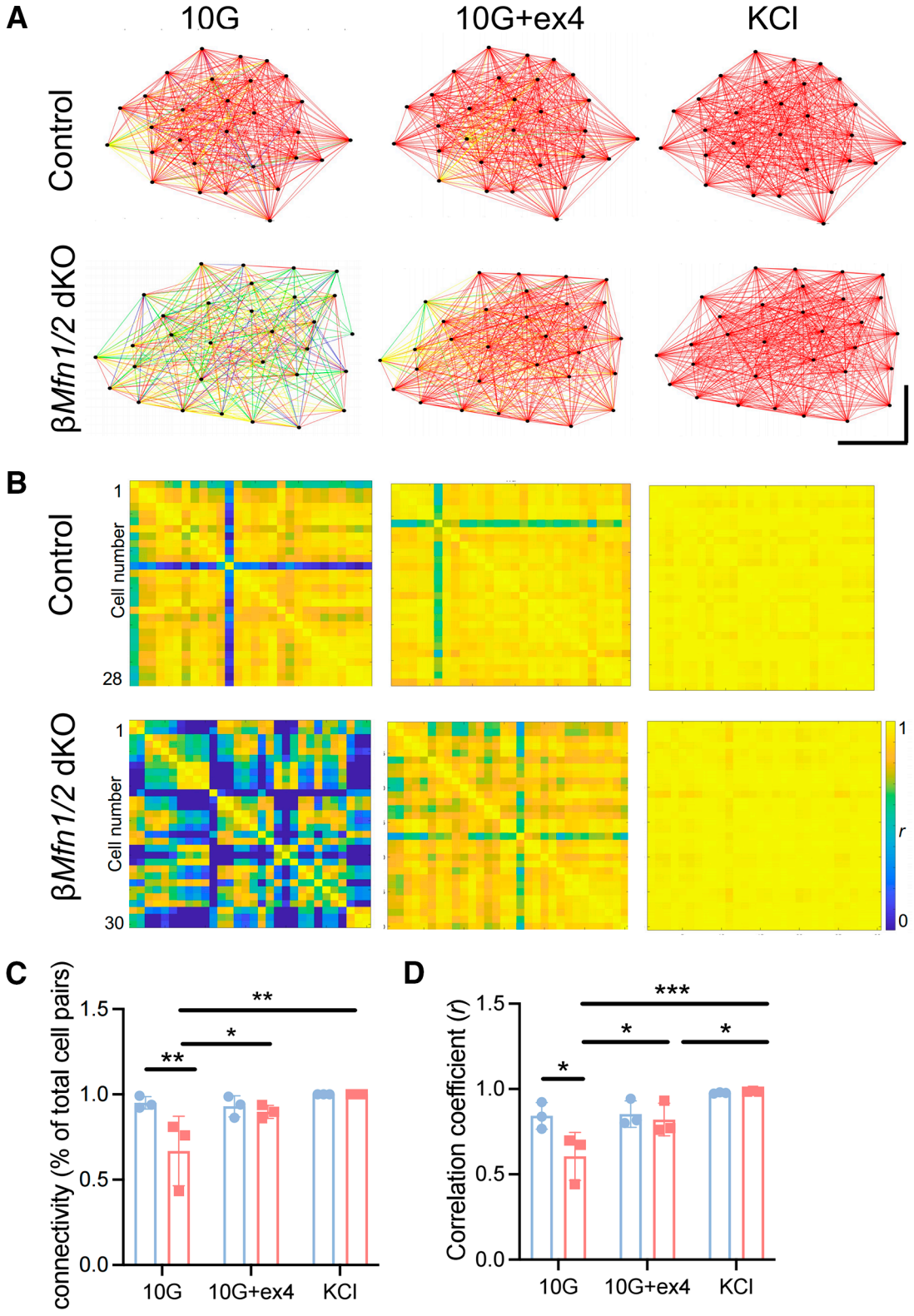

Figure 7—The GLP1-R agonist, exendin-4, improves intercellular connectivity in β*Mfn1/2*-dKO β-cells. *A*: Representative Cartesian maps of control and dKO islets with color-coded lines connecting cells according to the strength of Pearson analysis (color-coded *r* values from 0 to 1, blue to red, respectively) under 10 mmol/L (10G), 10G with 100 nmol/L exendin-4 (10G+ex4), or 20 mmol/L KCl; scale bars: 40 μm. *B*: Representative heat maps depicting connectivity strength (*r*) of all cell pairs according to the color-coded *r* values from 0 to 1, blue to yellow, respectively. *C*: Percentage of connected cell pairs at 10G, 10G+ex4, or KCl (n = 19–20 islets, three mice per genotype). D: The *r* values between β-cells in response to glucose, exendin-4, or KCl (n = 3 mice per genotype). Experiments were performed in 14-week-old male mice. Data are presented as mean ± SD. *$P < 0.05$,**$P < 0.01$, ***$P < 0.001$, assessed by two-way ANOVA test and the Šidák multiple comparisons test.

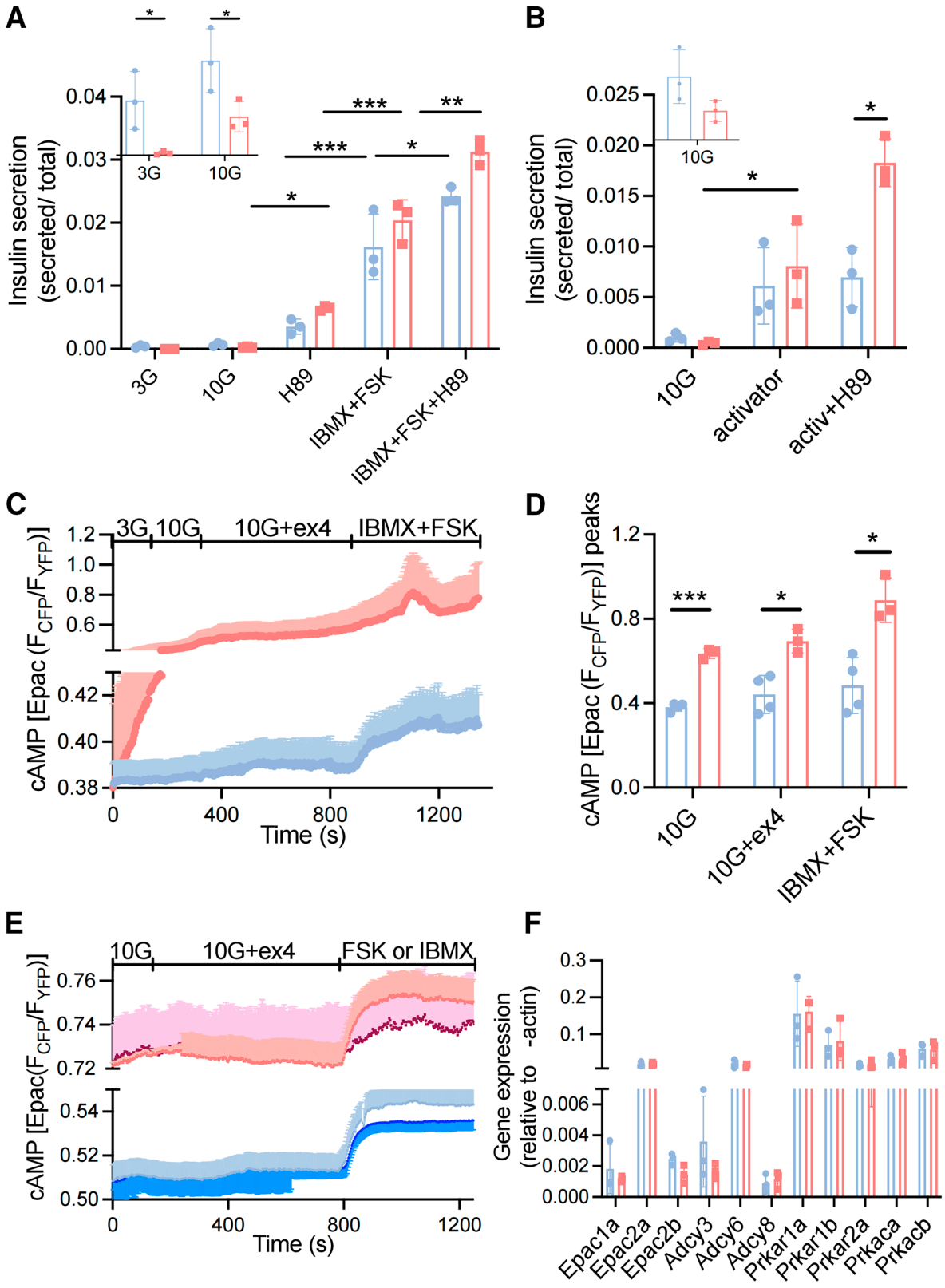

Figure 8—Insulin secretion is rescued through an EPAC-dependent activation in dKO islets. *A*: Insulin secretion measured during serial incubations in batches in 3 mmol/L glucose (3G), 10 mmol/L glucose (10G), or 10G supplemented with 10 μmol/L H89, or 10 μmol/l FSK with 100 μmol/l IBMX or H89 (n = 3 mice per genotype, in two independent experiments). *B*: Insulin secretion measured during serial incubations in batches in 10G, or 10G supplemented with 6 μmol/L EPAC-activator, or EPAC-activator with 10 μmol/L H89 (n = 3 mice per genotype, in two independent experiments). *C*: Representative Epac1-camps FRET traces in response to 3G or 10G, or 10G supplemented with 100 nmol/L exendin-4 (10G+ex4), or 10 μmol/l FSK with 100 μmol/l IBMX in dissociated β-cells. *D*: Fluorescence ratio peak values

the expression of *Epac*, *Adcy*, or *Prkar* (PKA) subunits were apparent between control and dKO islets (Fig. 8*F*).

Defective GSIS Is Rescued by GLP-1R Agonism in *Clec16a*-Null Mice

To determine whether incretins may reverse defective insulin secretion in an alternative model of mitochondrial dysfunction, we examined mice lacking the mitophagy regulator *Clec16a* selectively in the pancreatic islet ($Clec16a^{\Delta panc}$) (22). GSIS was sharply inhibited in null versus Pdx1-Cre control mice, and these differences between genotype were largely corrected in by the addition of exendin-4 (Supplementary Fig. 8*A*). Correspondingly, whereas the difference between $Clec16a^{\Delta panc}$ and control mice was significant for IPGTTs, there was no such (significant) difference for the OGTTs at 15 min, in line with the findings above for β*Mfn1/2*-dKO mice (Supplementary Fig. 8*A–C*).

Defective Secretion of a Preserved Pool of Morphologically Docked Granules in β*Mfn1/2*-dKO Mouse β-Cells

To determine whether the markedly weaker stimulation of insulin secretion in dKO islets may reflect failed recruitment of secretory granules into a readily releasable or morphologically docked pool beneath the plasma membrane, we next deployed total internal reflection fluorescence microscopy in dissociated β-cells. By overexpressing NPY-Venus, the number of insulin granules was significantly higher in close proximity with the plasma membrane in dKO cells after treatment with 20 mmol/L KCl (Supplementary Fig. 9*A* and *B*). However, when we then used ZIMIR (30) in response to depolarization as a surrogate for insulin secretion, release events were fewer in number and smaller in dKO (Supplementary Fig. 9*C–E*).

Altered Plasma Metabolomic and Lipidomic Profiles in β*Mfn1/2*-dKO Mice

We applied an -omics approach to study metabolite and lipid changes in peripheral plasma samples from control and dKO mice (Supplementary Fig. 10). Of 29 metabolites, the levels of five metabolic species (shown in red) were significantly altered in β*Mfn1/2*-dKO animals (Supplementary Fig. 10*A*). In the lipidomics analysis, the majority of lipid classes displayed a remarkably homogeneous downward trend in dKO samples (Supplementary Fig. 10*B*).

DISCUSSION

The key goal of the current study was to determine the role of mitofusins in controlling mitochondrial dynamics and hence glucose- and incretin-stimulated insulin secretion in the β-cell. Our strategy involved deleting both mitofusin isoforms since the expression of *Mfn1* and *Mfn2* is similar in the β-cell (47), suggestive of partial functional redundancy (48). Our measurements of *Mfn1* and *Mfn2* expression in mouse models of T2D nonetheless revealed changes in the expression of these genes, which may contribute to the disease.

Importantly, we show that *Mfn1* and *Mfn2* are critical regulators of the mitochondrial network in β-cells and consequently of insulin secretion in vitro and in vivo (see also [41]) (Supplementary Fig. 11*A* and *B*). These findings are in line with earlier studies, albeit involving the deletion of genes other than the mitofusins (13–18). Additionally, we show that changes in *Mfn1* and *Mfn2* expression occur in models of diabetes, and hence, their forced changes, as achieved in our study, may have relevance for the pathoetiology of β-cell failure in T2D and metabolic changes consistent with insulin deficiency. These include higher levels of bile acids as previously described in rodent models of type 1 diabetes (T1D) and T2D and in humans (49,50), elevated leucine and isoleucine, as observed in human T1D (51), and an altered triglyceride profile (52). Finally, these metabolomic/lipidomic data provide further support for the expected actions of mitofusin deletion via altered β-cell function, with changes that are somewhat more in line with metabolomic changes in human T1D (and models thereof) than T2D (53). Indeed, dKO mice gain less weight than controls as they show the classic symptoms of diabetes (54,55). This is likely to be the result of metabolic dyshomeostasis in the face of lowered circulating insulin levels, leading to impaired fat storage, loss of liver and muscle glycogen, and eventually, loss of muscle mass (i.e., the cardinal symptoms of T1D and of advanced insulin-requiring T2D in humans).

Of note, none of the earlier reports investigating the effects of mitochondrial disruption in the β-cell explored the effects on incretin-stimulated secretion. Suggesting a differential effect on glucose- versus incretin-stimulated secretion we show here; firstly, that insulin secretion and glucose excursion were less markedly affected by mitofusin knockout during OGTTs, where an incretin effect is preserved (56), than during IPGTTs. Correspondingly, insulin secretion stimulated by incretins was largely preserved in dKO cells, in contrast to the ablation of glucose-stimulated secretion (Supplementary Fig. 11*C* and *D*). Strikingly,

corresponding to *C* were measured between 200 and 250s (under 10G), 620 and 720s (under 10G with ex4) or 1,110 and 1,160s (under 10G with IBMX and FSK) (n = 3–4 mice per genotype, 15–35 cells in two independent experiments). *E*: Representative Epac1-camps FRET traces in response to 10G, 10G+ex4, 10 μmol/L FSK (dark blue or purple traces), or 100 μmol/L IBMX (light blue or pink traces) in dissociated β-cells (n = 3 mice per genotype, 15–45 cells). *F*: qRT-PCR quantification of *Epac, Adcy*, and *Prka* genes expression in control and dKO islets relative to *β-actin* (n = 3 mice per genotype in two independent experiments). Experiments were performed in 14-week-old male mice. Data are presented as mean ± SD. $^*P < 0.05$,$^{**}P < 0.01$, $^{***}P < 0.001$, assessed by two-way ANOVA test and the Šidák multiple comparisons test.

mitofusin deletion also enhanced incretin-stimulated cytosolic cAMP increases. That this effect was preserved in the face of phosphodiesterase inhibition (IBMX) and AC activation was surprising but may reflect an increase in total AC activity or distribution in dKO cells.

While PKA suppression is considered to be either neutral or inhibitory toward GSIS in wild-type β-cells (57–59), our data show a rather striking increase in insulin secretion in the presence of H89 in islets from mice of either genotype. While unexpected, and in contrast with those of others that support a role for PKA downstream of cAMP in the β-cell, Bryan and colleagues (57) provide some evidence for the stimulation of GSIS by H89 under certain conditions. Nevertheless, several studies have stressed the importance of both PKA-dependent and PKA-independent effects of increased $[cAMP]_i$ on GSIS from islets (60). Thus, PKA-independent exocytosis occurs through interactions between Epac-2/cAMP- guanine-nucleotide-exchange factor II (61,62), Rab3A, and Rim2 (proteins involved in vesicle trafficking [57,58, 63] and fusion) (64). On the other hand, GLUT2, Kir6.2, and SUR1, and α-SNAP (a vesicle-associated protein) have been reported to be phosphorylated by PKA (58). Here, we show that the effect of mitofusin deletion on GSIS is preserved when PKA is inhibited by H89 and even potentiated by EPAC-activation (Supplementary Fig. 11*C* and *D*). These changes appear to be exerted at the posttranscriptional level, since we observed no changes in levels of mRNAs encoding the relevant β-cell isoforms of *Epac*. Whether there are changes in the level or the corresponding proteins including EPAC, their subcellular localization or interaction with upstream regulators or downstream effectors, remains to be explored. Finally, the latter findings could indicate that an intact mitochondrial reticulum restricts signaling by EPAC through a mechanism that is inhibited by PKA. Future studies, using additional or alternative PKA inhibitors (65), will be needed to explore these possibilities.

Possibly contributing to these differences in the effects on responses to glucose versus incretin, exendin-4 treatment led to greater Ca^{2+} accumulation in the ER in dKO cells. By enhancing Ca^{2+} cycling across the ER membrane, this could conceivably drive larger local increases in cytosolic Ca^{2+}, which, in turn, may influence plasma membrane potential, trigger Ca^{2+} influx via VDCCs, and hence, stimulate insulin release (66).

We also demonstrate that preserved mitochondrial ultrastructure is critical for normal β-cell–β-cell connectivity, itself required for normal insulin secretion (41,67). The mechanisms underlying impaired connectivity in the absence of mitofusins are unclear but may involve altered *Cx36/Gjd2* expression, phosphorylation, or activity impacting gap junctions (42).

In summary, we show that acute treatment with incretins, commonly used as treatments for T2D and obesity (56), largely reverses the deficiencies in insulin secretion that follow mitochondrial disruption. Future studies will be needed to address the relevance of these findings to human β-cells and to the action of incretins in clinical settings.

Acknowledgments. The authors thank Stephen M. Rothery, from the Facility for Imaging by Light Microscopy (FILM) at Imperial College London, for support with confocal and widefield microscopy image recording and analysis. The authors thank Professor Julia Gorelik and Sasha Judina (Imperial College) for providing the Epac1-camps sensor, and Aida Di Gregorio from the National Heart and Lung Institute (Imperial College) for genotyping the mice.

Funding. G.A.R. was supported by a Wellcome Trust Senior Investigator Award (098424AIA) and Wellcome Trust Investigator Award (212625/Z/18/Z), Medical Research Council Programme grants (MR/R022259/1, MR/J0003042/1, MR/L020149/1), an Experimental Challenge Grant (DIVA, MR/L02036X/1), a Medical Research Council grant (MR/N00275X/1), and Diabetes UK grants (BDA/11/0004210, BDA/15/0005275, BDA16/0005485). I.L. was supported by a Diabetes UKD project grant (16/0005485). This project has received funding from the European Commission Innovative Medicines Initiative 2 Joint Undertaking, under grant agreement no. 115881 (RHAPSODY). This Joint Undertaking receives support from the European Union's Horizon 2020 Research and Innovation Programme. This work is supported by the Swiss State Secretariat for Education, Research and Innovation (SERI), under contract no. 16.0097. A.T. was supported by Medical Research Council project grant MR/R010676/1. Intravital imaging was performed using resources and/or funding provided by National Institutes of Health grants R03 DK115990 (to A.K.L.), Human Islet Research Network UC4 DK104162 (to A.K.L., RRID:SCR_014393). BJ acknowledges support from the Academy of Medical Sciences, Society for Endocrinology, The British Society for Neuroendocrinology, the European Federation for the Study of Diabetes, an Engineering and Physical Sciences Research Council capital award, and the Medical Research Council (MR/R010676/1). S.A.S. was supported by the JDRF (CDA-2016-189, SRA-2018-539, COE-2019-861), the National Institutes of Health (R01 DK108921, U01 DK127747), and the U.S. Department of Veterans Affairs (I01 BX004444).

Duality of Interest. This Joint Undertaking receives support from the European Federation of Pharmaceutical Industries and Associations. G.A.R. has received grant funding and consultancy fees from Les Laboratoires Servier and Sun Pharmaceuticals. No other potential conflicts of interest relevant to this article were reported.

Author Contributions. E.G. performed experiments and analyzed data. E.G. supported the completion of confocal and widefield microscopy and analysis. E.G. contributed to designing the study and writing the manuscript C.M., M.M., and A.K.L. were responsible for the in vivo intravital Ca^{2+} imaging in mice presented in the bioRxiv paper [41]. P.C. contributed to the analysis and manipulation of the in vivo intravital Ca^{2+} measurements as well as the preparation and imaging of total internal reflection fluorescence samples. E.A. and L.L.N. performed the oral gavage in live animals. A.T. performed the electron microscopy sample processing and data analysis. F.Y.S.W. and Y.A. generated and performed Monte Carlo-based signal binarization. T.S. contributed to the generation of the MATLAB script used for connectivity analysis. A.W. and C.L.-Q. contributed to the metabolomics analysis. B.J. assisted with the cAMP assays. Y.X. and G.G. performed studies with the Pdx1CreER mice. N.A. assisted with Seahorse experiment protocols. C.C.-G., C.M., and M.I. were responsible for the RNA sequencing data analysis. I.L. and T.A.R. were responsible for the maintenance of mouse colonies and final approval of the version to be published. S.A.S. performed studies with Clec16a mice. T.A.R. was involved in the design of the floxed *Mfn* alleles. G.A.R. designed the study and wrote the manuscript with input and final approval of the version to be published from all authors. G.A.R. is the guarantor of this work and, as such, had full access to all the data in the study and takes responsibility for the integrity of the data and the accuracy of the data analysis.

Prior Presentation. Parts of this study were presented as an oral or poster presentation at the 81st Scientific Sessions of the American Diabetes Association, virtual meeting, 25–29 June 2021; the Australasian Diabetes Congress 2021, virtual event, 11–13 August 2021; the 80th Scientific Sessions of the American Diabetes Association, virtual meeting, 12–16 June 2020; Diabetes UK Professional Conference 2019, Liverpool, U.K., 6–8 March 2019; Gordon Research Conference, New London, NH, 19–22 March 2019; Rhapsody Consortium; and the 54th Annual Meeting of the European Association for the Study of Diabetes, Berlin, Germany, 1–5 October 2018. A non–peer-reviewed version of this article was published on the bioRxiv preprint server (https://doi.org/10.1101/2020.04.22.055384) on 24 April 2020.

References

1. Anderson AJ, Jackson TD, Stroud DA, Stojanovski D. Mitochondria-hubs for regulating cellular biochemistry: emerging concepts and networks. Open Biol 2019;9:190126
2. Rutter GA, Pullen TJ, Hodson DJ, Martinez-Sanchez A. Pancreatic β-cell identity, glucose sensing and the control of insulin secretion. Biochem J 2015;466:203–218
3. Rorsman P, Ashcroft FM. Pancreatic β-cell electrical activity and insulin secretion: of mice and men. Physiol Rev 2018;98:117–214
4. Henquin JC. Triggering and amplifying pathways of regulation of insulin secretion by glucose. Diabetes 2000;49:1751–1760
5. Jones B, Bloom SR, Buenaventura T, Tomas A, Rutter GA. Control of insulin secretion by GLP-1. Peptides 2018;100:75–84
6. Yang D, Ying J, Wang X, et al. Mitochondrial dynamics: a key role in neurodegeneration and a potential target for neurodegenerative disease. Front Neurosci 2021;15:654785
7. Rutter GA, Rizzuto R. Regulation of mitochondrial metabolism by ER Ca2+ release: an intimate connection. Trends Biochem Sci 2000;25:215–221
8. Westermann B. Bioenergetic role of mitochondrial fusion and fission. Biochim Biophys Acta 2012;1817:1833–1838
9. Ma K, Chen G, Li W, Kepp O, Zhu Y, Chen Q. Mitophagy, mitochondrial homeostasis, and cell fate. Front Cell Dev Biol 2020;8:467
10. Filadi R, Greotti E, Turacchio G, Luini A, Pozzan T, Pizzo P. On the role of mitofusin 2 in endoplasmic reticulum-mitochondria tethering. Proc Natl Acad Sci U S A 2017;114:E2266–E2267
11. Rovira-Llopis S, Bañuls C, Diaz-Morales N, Hernandez-Mijares A, Rocha M, Victor VM. Mitochondrial dynamics in type 2 diabetes: pathophysiological implications. Redox Biol 2017;11:637–645
12. Serasinghe MN, Chipuk JE. Mitochondrial fission in human diseases. Handb Exp Pharmacol 2017;240:159–188
13. Reinhardt F, Schultz J, Waterstradt R, Baltrusch S. Drp1 guarding of the mitochondrial network is important for glucose-stimulated insulin secretion in pancreatic beta cells. Biochem Biophys Res Commun 2016;474:646–651
14. Hennings TG, Chopra DG, DeLeon ER, et al. In vivo deletion of β-cell Drp1 impairs insulin secretion without affecting islet oxygen consumption. Endocrinology 2018;159:3245–3256
15. Supale S, Thorel F, Merkwirth C, et al. Loss of prohibitin induces mitochondrial damages altering β-cell function and survival and is responsible for gradual diabetes development. Diabetes 2013;62:3488–3499
16. Stiles L, Shirihai OS. Mitochondrial dynamics and morphology in beta-cells. Best Pract Res Clin Endocrinol Metab 2012;26:725–738
17. Zhang Z, Wakabayashi N, Wakabayashi J, et al. The dynamin-related GTPase Opa1 is required for glucose-stimulated ATP production in pancreatic beta cells. Mol Biol Cell 2011;22:2235–2245
18. Men X, Wang H, Li M, et al. Dynamin-related protein 1 mediates high glucose induced pancreatic beta cell apoptosis. Int J Biochem Cell Biol 2009;41:879–890
19. Del Guerra S, Lupi R, Marselli L, et al. Functional and molecular defects of pancreatic islets in human type 2 diabetes. Diabetes 2005;54:727–735
20. Chen H, McCaffery JM, Chan DC. Mitochondrial fusion protects against neurodegeneration in the cerebellum. Cell 2007;130:548–562
21. Gu G, Dubauskaite J, Melton DA. Direct evidence for the pancreatic lineage: NGN3+ cells are islet progenitors and are distinct from duct progenitors. Development 2002;129:2447–2457
22. Soleimanpour SA, Gupta A, Bakay M, et al. The diabetes susceptibility gene Clec16a regulates mitophagy. Cell 2014;157:1577–1590
23. Ravier MA, Rutter GA. Isolation and culture of mouse pancreatic islets for ex vivo imaging studies with trappable or recombinant fluorescent probes. Methods Mol Biol 2010;633:171–184
24. Georgiadou E, Haythorne E, Dickerson MT, et al. The pore-forming subunit MCU of the mitochondrial Ca^{2+} uniporter is required for normal glucose-stimulated insulin secretion in vitro and in vivo in mice. Diabetologia 2020;63:1368–1381
25. Kolesar JE, Wang CY, Taguchi YV, Chou SH, Kaufman BA. Two-dimensional intact mitochondrial DNA agarose electrophoresis reveals the structural complexity of the mammalian mitochondrial genome. Nucleic Acids Res 2013;41:e58
26. Ravier MA, Daro D, Roma LP, et al. Mechanisms of control of the free Ca2+ concentration in the endoplasmic reticulum of mouse pancreatic β-cells: interplay with cell metabolism and [Ca2+]c and role of SERCA2b and SERCA3. Diabetes 2011;60:2533–2545
27. Varadi A, Rutter GA. Dynamic imaging of endoplasmic reticulum Ca2+ concentration in insulin-secreting MIN6 Cells using recombinant targeted cameleons: roles of sarco(endo)plasmic reticulum Ca2+-ATPase (SERCA)-2 and ryanodine receptors. Diabetes 2002;51(Suppl. 1):S190–S201
28. Nikolaev VO, Bünemann M, Hein L, Hannawacker A, Lohse MJ. Novel single chain cAMP sensors for receptor-induced signal propagation. J Biol Chem 2004;279:37215–37218
29. Wiemerslage L, Lee D. Quantification of mitochondrial morphology in neurites of dopaminergic neurons using multiple parameters. J Neurosci Methods 2016;262:56–65
30. Li D, Chen S, Bellomo EA, et al. Imaging dynamic insulin release using a fluorescent zinc indicator for monitoring induced exocytotic release (ZIMIR). Proc Natl Acad Sci U S A 2011;108:21063–21068
31. Tsuboi T, Rutter GA. Multiple forms of "kiss-and-run" exocytosis revealed by evanescent wave microscopy. Curr Biol 2003;13:563–567
32. Ahonen L, Jäntti S, Suvitaival T, et al. Targeted clinical metabolite profiling platform for the stratification of diabetic patients. Metabolites 2019;9:184
33. Taddeo EP, Alsabeeh N, Baghdasarian S, et al. Mitochondrial proton leak regulated by cyclophilin D elevates insulin secretion in islets at nonstimulatory glucose levels. Diabetes 2020;69:131–145
34. Brand MD, Nicholls DG. Assessing mitochondrial dysfunction in cells. Biochem J 2011;435:297–312
35. Carrat GR, Haythorne E, Tomas A, et al. The type 2 diabetes gene product STARD10 is a phosphoinositide-binding protein that controls insulin secretory granule biogenesis. Mol Metab 2020;40:101015
36. Akalestou E, Suba K, Lopez-Noriega L, et al. Intravital imaging of islet Ca^{2+} dynamics reveals enhanced β cell connectivity after bariatric surgery in mice. Nat Commun 2021;12:5165
37. Cruciani-Guglielmacci C, Bellini L, Denom J, et al. Molecular phenotyping of multiple mouse strains under metabolic challenge uncovers a role for *Elovl2* in glucose-induced insulin secretion. Mol Metab 2017;6:340–351
38. Benjamini Y, Hochberg Y. Controlling the false discovery rate: a practical and powerful approach to multiple testing. J R Stat Soc B 1995;57:289–300
39. Elayat AA, el-Naggar MM, Tahir M. An immunocytochemical and morphometric study of the rat pancreatic islets. J Anat 1995;186:629–637
40. Pullen TJ, Huising MO, Rutter GA. Analysis of purified pancreatic islet beta and alpha cell transcriptomes reveals 11β-hydroxysteroid dehydrogenase (Hsd11b1) as a novel disallowed gene. Front Genet 2017;8:41
41. Georgiadou E, Muralidharan C, Martinez M, et al. Mitofusins *Mfn1* and *Mfn2* are required to preserve glucose but not incretin-stimulated beta cell connectivity and insulin secretion. 13 August 2021 [preprint]. bioRxiv:2020.04.22.055384

42. Rutter GA, Georgiadou E, Martinez-Sanchez A, Pullen TJ. Metabolic and functional specialisations of the pancreatic beta cell: gene disallowance, mitochondrial metabolism and intercellular connectivity. Diabetologia 2020;63: 1990–1998
43. Johnston NR, Mitchell RK, Haythorne E, et al. Beta cell hubs dictate pancreatic islet responses to glucose. Cell Metab 2016;24:389–401
44. Gautam D, Han SJ, Hamdan FF, et al. A critical role for beta cell M3 muscarinic acetylcholine receptors in regulating insulin release and blood glucose homeostasis in vivo. Cell Metab 2006;3:449–461
45. Gautam D, Ruiz de Azua I, Li JH, et al. Beneficial metabolic effects caused by persistent activation of beta-cell M3 muscarinic acetylcholine receptors in transgenic mice. Endocrinology 2010;151:5185–5194
46. Gembal M, Gilon P, Henquin JC. Evidence that glucose can control insulin release independently from its action on ATP-sensitive K+ channels in mouse B cells. J Clin Invest 1992;89:1288–1295
47. Benner C, van der Meulen T, Cacéres E, Tigyi K, Donaldson CJ, Huising MO. The transcriptional landscape of mouse beta cells compared to human beta cells reveals notable species differences in long non-coding RNA and protein-coding gene expression. BMC Genomics 2014;15:620
48. Sidarala V, Zhu J, Pearson GL, Reck EC, Kaufman BA, Soleimanpour SA. Mitofusins 1 and 2 collaborate to fuel pancreatic beta cell insulin release via regulation of both mitochondrial structure and DNA content. 11 January 2021 [preprint]. bioRxiv 2021.01.10.426151.
49. Andersén E, Karlaganis G, Sjövall J. Altered bile acid profiles in duodenal bile and urine in diabetic subjects. Eur J Clin Invest 1988;18:166–172
50. Uchida K, Makino S, Akiyoshi T. Altered bile acid metabolism in nonobese, spontaneously diabetic (NOD) mice. Diabetes 1985;34:79–83
51. Sailer M, Dahlhoff C, Giesbertz P, et al. Increased plasma citrulline in mice marks diet-induced obesity and may predict the development of the metabolic syndrome. PLoS One 2013;8:e63950
52. Lamichhane S, Ahonen L, Dyrlund TS, et al. Dynamics of plasma lipidome in progression to islet autoimmunity and type 1 diabetes - Type 1 Diabetes Prediction and Prevention Study (DIPP). Sci Rep 2018;8:10635
53. George AM, Jacob AG, Fogelfeld L. Lean diabetes mellitus: an emerging entity in the era of obesity. World J Diabetes 2015;6:613–620
54. Mitchell RK, Nguyen-Tu MS, Chabosseau P, et al. The transcription factor *Pax6* is required for pancreatic β cell identity, glucose-regulated ATP synthesis, and Ca^{2+} dynamics in adult mice. J Biol Chem 2017;292: 8892–8906
55. Martinez-Sanchez A, Nguyen-Tu M-S, Rutter GA. DICER Inactivation Identifies Pancreatic β-Cell "Disallowed" Genes Targeted by MicroRNAs. Mol Endocrinol 2015;29:1067–1079
56. Nauck MA, Quast DR, Wefers J, Meier JJ. GLP-1 receptor agonists in the treatment of type 2 diabetes - state-of-the-art. Mol Metab 2021;46:101102
57. Nakazaki M, Crane A, Hu M, et al. cAMP-activated protein kinase-independent potentiation of insulin secretion by cAMP is impaired in SUR1 null islets. Diabetes 2002;51:3440–3449
58. Kashima Y, Miki T, Shibasaki T, et al. Critical role of cAMP-GEFII–Rim2 complex in incretin-potentiated insulin secretion. J Biol Chem 2001;276:46046–46053
59. Chepurny OG, Kelley GG, Dzhura I, et al. PKA-dependent potentiation of glucose-stimulated insulin secretion by Epac activator 8-pCPT-2′-O-Me-cAMP-AM in human islets of Langerhans. Am J Physiol Endocrinol Metab 2010;298:E622–E633
60. Renström E, Eliasson L, Rorsman P. Protein kinase A-dependent and -independent stimulation of exocytosis by cAMP in mouse pancreatic B-cells. J Physiol 1997;502:105–118
61. de Rooij J, Zwartkruis FJ, Verheijen MH, et al. Epac is a Rap1 guanine-nucleotide-exchange factor directly activated by cyclic AMP. Nature 1998;396:474–477
62. Kawasaki H, Springett GM, Mochizuki N, et al. A family of cAMP-binding proteins that directly activate Rap1. Science 1998;282:2275–2279
63. Ozaki N, Shibasaki T, Kashima Y, et al. cAMP-GEFII is a direct target of cAMP in regulated exocytosis. Nat Cell Biol 2000;2:805–811
64. Wang Y, Perfetti R, Greig NH, et al. Glucagon-like peptide-1 can reverse the age-related decline in glucose tolerance in rats. J Clin Invest 1997;99:2883–2889
65. Lochner A, Moolman JA. The many faces of H89: a review. Cardiovasc Drug Rev 2006;24:261–274
66. Gilon P, Arredouani A, Gailly P, Gromada J, Henquin JC. Uptake and release of Ca2+ by the endoplasmic reticulum contribute to the oscillations of the cytosolic Ca2+ concentration triggered by Ca2+ influx in the electrically excitable pancreatic B-cell. J Biol Chem 1999;274:20197–20205
67. Salem V, Silva LD, Suba K, et al. Leader β-cells coordinate Ca^{2+} dynamics across pancreatic islets in vivo. Nat Metab 2019;1:615–629